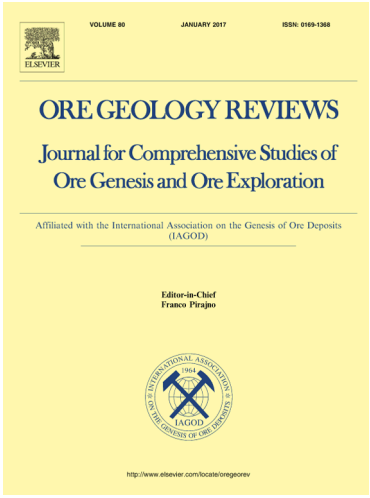

Magmatic evolution and porphyry–epithermal mineralization in the Taftan volcanic complex, southeastern Iran

Jeremy P. Richards, Amir M. Razavi, Terry L. Spell, Andrew Locock, Ali Sholeh, Mehraj Aghazadeh

PII: S0169-1368(17)30857-0
DOI: https://doi.org/10.1016/j.oregeorev.2018.02.018
Reference: OREGEO 2497

To appear in: *Ore Geology Reviews*

Received Date: 9 November 2017
Revised Date: 5 February 2018
Accepted Date: 12 February 2018

Please cite this article as: J.P. Richards, A.M. Razavi, T.L. Spell, A. Locock, A. Sholeh, M. Aghazadeh, Magmatic evolution and porphyry–epithermal mineralization in the Taftan volcanic complex, southeastern Iran, *Ore Geology Reviews* (2018), doi: https://doi.org/10.1016/j.oregeorev.2018.02.018

Magmatic evolution and porphyry–epithermal mineralization in the Taftan volcanic complex, southeastern Iran

Jeremy P. Richards[1,2,*], Amir M. Razavi[1], Terry L. Spell[3], Andrew Locock[1], Ali Sholeh[4], Mehraj Aghazadeh[5]

[1]Department of Earth & Atmospheric Sciences, University of Alberta, Edmonton, Alberta, T6G 2E3, Canada

[2] Mineral Exploration Research Centre, Harquail School of Earth Sciences, Laurentian University, 935 Ramsey Lake Road, Sudbury, Ontario, P3E 2C6, Canada

[3]Department of Geoscience, University of Nevada, Las Vegas, 4505 Maryland Parkway, Las Vegas, NV, 89154-4010, USA

[4]Department of Geology, Faculty of Basic Sciences, Tarbiat Modares University, Tehran, Iran

[5]Department of Geology, Payame Noor University, Tabriz, Iran

* e-mail: JRichards2@laurentian.ca

Abstract

The Taftan volcanic complex is located above the Makran subduction zone in Sistan and Baluchestan province, southeastern Iran. The earliest volcanic activity at Taftan started in the late Miocene (~8 Ma) with eruption of andesitic to dacitic lava onto a Cretaceous to Eocene volcanic and sedimentary paleosurface ~20 km to the northwest of the current volcanic edifice. Later Plio-Pleistocene volcanism consisted of voluminous andesitic and dacitic lavas and pyroclastic flows (~3.1 to 0.4 Ma). Taftan, and the neighbouring Bazman volcano, are the southeasternmost and youngest manifestations of arc-related volcanism in Iran, which began with the Eocene–Miocene Urumieh-Dokhtar Magmatic Arc (UDMA) in northwest and central Iran, and extends into western Pakistan (Chagai Arc).

Major porphyry Cu±Mo±Au deposits are associated with Miocene to Pliocene intrusive rocks in the Kerman section of the Eocene–Neogene Urumieh-Dokhtar Magmatic Arc in southeastern Iran (e.g., Sar Cheshmeh, Meiduk), and at Reko Diq and Saindak in the Late Cretaceous–Quaternary Chagai Arc in western Pakistan. In a gap of ~300 km between these two belts, several porphyry and epithermal prospects are exposed in the Miocene–Pliocene sections of the Taftan volcanic complex, including the Kharestan (6.10 ± 0.80 Ma) and Bidester porphyry-epithermal Cu-Au deposits (~4.3 Ma), and the Siah Jangal epithermal Au deposit (late Miocene). In addition, several argillic to advanced argillic and fumarolic alteration zones occur in Plio-Pleistocene volcanic rocks around the current volcanic edifice. These deposits have received limited exploration.

Electron microprobe analyses of amphibole (magnesio-hastingsite) phenocrysts and magnetite–ilmenite mineral pairs from the Taftan and Bazman volcanic rocks indicate a change of crystallization temperature and magmatic oxidation state from ~1000°C and $\Delta FMQ \approx +1$ in andesitic rocks, to ~900°C and $\Delta FMQ \approx +2$ in dacitic rocks. Magmatic water content was >4 wt.%, as indicated by the ubiquitous presence of amphibole phenocrysts.

Major and trace element compositions of the Taftan and Bazman volcanic rocks show calc-alkaline to high-K calc-alkaline affinity, with relative depletions of Nb, Ta, and Ti and enrichments of large-ion lithophile elements (LILE), Th, and U on normalized diagrams. These trace element patterns, including listric-shaped normalized rare earth element profiles and relatively high Sr/Y and La/Yb ratios, are similar to those of fertile Miocene igneous rocks from the Kerman Belt and Chagai Arc, and suggest that the Taftan suite in particular should be prospective for porphyry Cu ore formation.

Regionally, there is no clear geochemical difference between the Neogene Kerman Belt rocks, which are thought to post-date the onset of collision between the Afro-Arabian and Eurasian plates (late Oligocene to earliest Miocene), and the subduction-related Bazman–Taftan and Chagai Belt magmas. The porphyry deposits formed in these distinct settings are also virtually indistinguishable. This suggests that most of the processes affecting the geochemistry and metallogeny of the magmas in both settings take place in the lithosphere, albeit that the ultimate source of the magmas is in the supra-subduction zone asthenospheric mantle wedge. In collisional environments, subduction-related material previously crystallized in the deep lithosphere is simply being remobilized.

Keywords: Stratovolcano, Iran, Makran, Neogene, Quaternary, porphyry copper deposit, epithermal gold deposit

1. Introduction

The Taftan volcanic complex (TVC) is located ~100 km south-southeast of Zahedan in Sistan and Baluchestan province, southeastern Iran (Figs. 1–3). It was constructed over the last 8 m.y. by a series of vents stepping progressively to the ESE to cover an area of ~57 x 29 km. Volcanism is currently centred on the easternmost vent, Madarkuh (4050 m above sea level; 28°35’56.3” N, 61°07’55.1” E), which is fumarolically active.

McCall (1997) suggested that the TVC is one of a chain of volcanic centers (including Bazman 150 km to the southwest, and Koh-i-Sultan 200 km to the east-northeast in the Chagai Hills of western Pakistan) that was developed on the northern border of the Makran Arc, in response to northward subduction of Arabian plate ocean lithosphere (Fig. 2).

Several previous studies have investigated the petrology, geochemistry, and tectonic evolution of the Makran Arc (e.g., Berberian and Berberian, 1981; Biabangard and Moradian, 2008; Perelló et al., 2008; Saadat and Stern, 2011). Pang et al. (2014) presented analyses of volcanic rocks from Taftan and Bazman, and Firouzkouhi et al. (2017) discussed evidence for magma mixing at Bazman. The purpose of this study is to understand the tectonomagmatic history and porphyry–epithermal mineralization potential of the TVC by synthesizing new and existing geochronological, geochemical, and mineral chemistry data. Some samples were also collected from the Bazman volcano for comparative purposes.

2. Regional Geological and Metallogenic Setting of the Taftan and Bazman Volcanic Complexes

The Taftan and Bazman stratovolcanic complexes in southeastern Iran, and the Koh-i-Sultan volcano in western Pakistan, are three of several Quaternary volcanic centres along the Neotethyan orogenic belt of Turkey–Iran–Pakistan, reflecting different stages of convergence from active subduction beneath the Makran, to advanced continental collision in northwest Iran and eastern Turkey (e.g., the Sahand, Sabalan, and Damavand stratovolcanoes; Fig. 1). In addition to these intermediate-composition volcanic complexes, widespread but scattered eruption of mafic alkaline lavas from monogenetic vents likely reflects lithospheric mantle melting during post-collisional stress relaxation or localized extension (Ahmadzadeh et al., 2010; Allen et al., 2013; Kheirkhah et al., 2013; Pang et al., 2013).

The large intermediate composition volcanic centres are harder to constrain in terms of their tectonic origin. Several of these volcanoes have mildly alkaline characteristics, and are ascribed to post-collisional crustal melting, perhaps in response to mantle lithosphere delamination (e.g., Davidson et al., 2004; Liotard et al., 2008; Mirnejad et al., 2010). The Bazman, Taftan, and Koh-i-Sultan volcanoes, however, have typical calc-alkaline arc-like compositions, and appear to be related to continued subduction of oceanic lithosphere beneath the Makran accretionary zone (Fig. 2; Gansser, 1971; Jacob and Quittmeyer, 1979; Biabangard and Moradian, 2008).

Of interest in this study is the occurrence of porphyry Cu and epithermal Au mineralization in the TVC (the late Miocene Kharestan and early Pliocene Bidester porphyry–epithermal Cu-Au prospects, and the Siah Jangal epithermal Au deposit), and the location of these deposits between the major Miocene Saindak and Reko Diq porphyry Cu-Au deposits of the Chagai arc in western Pakistan, and the numerous large Miocene porphyry Cu deposits of the Kerman Belt of southeastern Iran (including the Sar Cheshmeh and Meiduk deposits). A direct link between the Chagai Arc and the Kerman Belt (part of the Cenozoic Urumieh-Dokhtar Magmatic Arc; UDMA; Fig. 1) has long been suspected, but the geodynamic settings appear distinct. Here we explore these similarities and differences.

2.1. The Makran Zone

Volcanism in SE Iran and SW Pakistan began in the Late Cretaceous and continues to the present day by consumption of oceanic lithosphere beneath the Makran and Chagai Arcs,

respectively (Byrne et al., 1992; Siddiqui et al., 2007). The present-day lateral transition from continent–continent collision in the Zagros Orogenic Belt to subduction below the Makran (at ~57° E; Fig. 2) is marked by a gravity contrast between the Zagros Orogen (negative anomaly) and the Makran Zone (positive anomaly; Ravaut et al., 1997).

The east–west-trending Makran Zone is a convergent margin, extending approximately 800 km from the Strait of Hormoz in Iran toward Karachi Harbour in Pakistan (Fig. 2; Aubourg et al., 2004). At the eastern margin, the Makran Zone is separated from the Indian plate by the dextral strike slip Ornach-Nal–Chaman fault (Fig. 2; Kukowski et al., 2000). This fault originated in the late Oligocene to early Miocene and continues to be active today (Wellman, 1966; Lawrence et al., 1992). The western border of the Makran Zone is marked by a ~30 km-wide zone of NNE–SSW-trending sinistral strike-slip faults, including the Zendan-Minab-Palami fault (Fig. 2; Regard et al., 2004; Bayer et al., 2006).

Whitmarsh (1979) suggested that subduction beneath the Makran Zone has been active since the Mesozoic, whereas Mountain and Prell (1990) suggested a Cenozoic age for the onset of subduction. However, the majority of researchers consider that subduction below the Makran Zone has been active since the Late Cretaceous and continues to the present time (Farhoudi and Karig, 1977; McCall, 2002; Bayer et al., 2006; Musson, 2009). The convergence rate varies from 25 mm/year in the western Makran to 30 mm/year in the east (Ellouz-Zimmermann et al., 2007; Grando and McClay, 2007).

The Makran Zone is tectonically subdivided into northern and southern basins (Arshadi and Förster, 1983; Shahabpour, 2010). The northern part is characterized as a forearc basin by the occurrence of several depressions (the large alluvial plains of Jaz Murian and Mashkhel; Fig. 2; Falcon, 1974). The southern part marks the base of the continental slope where shelf sediments including flysch to neritic and molassic sediments have been deposited, and is known as the Makran Accretionary Prism (Farhoudi and Karig, 1977; Arshadi and Förster, 1983; Fig. 2). To the north of the Jaz Murian depression, Cenozoic volcanoplutonic rocks are mainly andesitic in composition and form the volcanic arc of the Makran subduction zone, which overlies Paleozoic metamorphosed sedimentary basement (Figs. 2 and 3; Falcon, 1974; Farhoudi and Karig, 1977). The volcanic centers include Bazman and Taftan in Iran (located ~300–400 km inland from the coast), and Koh-i-Sultan in the Chagai arc of Pakistan (~450 km from the coast; Fig. 3).

Pang et al. (2014) have summarized the tectonic and geochemical evolution of the western Makran volcanic arc based on major and trace elements, Sr-Nd isotopes, and U-Pb

dating. They suggested that Neogene arc magmatism in the Makran likely started in the early Miocene (19.0 ± 0.2 Ma; Mirabad pluton) and continued to the late Pleistocene (0.84 ± 0.06 Ma; Taftan andesitic rocks); our new age dating at Taftan extends this range to 0.4 Ma (see §6 below). The Taftan volcanic rocks have εNd and $^{87}Sr/^{86}Sr$ values ranging from -4.4 to -3.0 (average = -3.4 ± 0.5) and from 0.704359 to 0.706760 (average = 0.7061 ± 0.0009) respectively (Pang et al., 2014). According to these results and trace element geochemistry, Pang et al. (2014) proposed that magmas in the Makran arc were derived from subduction-modified mantle, and have evolved through a combination of crustal assimilation and fractional crystallization processes.

Several large porphyry Cu-Au deposits (Reko Diq: 2.2 Gt @ 0.53% Cu, 0.30 g/ton Au; Saindak: 440 Mt @ 0.41% Cu, 0.002% Mo; Sillitoe and Khan, 1977; Sillitoe, 1979; Perelló et al., 2008; Richards et al., 2012; Richards and Sholeh, 2016) and smaller prospects have been reported in the eastern Makran, but only a few partially explored deposits such as the Kharestan and Bidester porphyry-epithermal Cu-Au deposits (see §3.2.1) and the Chahnaly low-sulfidation epithermal Au deposit to the north of Bazman (Sholeh et al., 2016) are known in the western Makran in Iran.

3. Geology of the Taftan volcanic complex

3.1. Volcanic sequence

The Taftan volcanic complex (Figs. 4, 5A) formed from the late Miocene to Quaternary, and overlies Late Cretaceous to Eocene volcanic and sedimentary rocks. The sedimentary units include flysch type deposits and fossiliferous (*Nummulites* and *Alveolinides*) limestones of Eocene age. The underlying Late Cretaceous volcanic sequences consist of ultramafic to mafic units of ophiolitic mélange (McCall, 1997; Biabangard and Moradian, 2008).

Volcanism at Taftan began in the late Miocene (~8 Ma; see below) with eruption of dacitic to andesitic lava flows and pyroclastic materials, and deposition of lahars, centered on an area ~30 km WNW of the current edifice (Fig. 5B). Thick (up to ~50 m) lahar deposits fill paleo-valleys to the south of Kharestan (Fig. 4).

The locus of volcanism shifted east-southeastward toward the current Taftan edifice in the Quaternary, with the eruption of lava flows and pyroclastic materials (Figs. 4, 5A,C). The extensive andesite lava flows retain much of their original morphology and texture. Pyroclastic deposits are mostly pumiceous andesitic ignimbrites with andesitic and dacitic clasts from the previous eruptions, and cover large areas on the distal eastern and

southeastern flanks of the volcano, extending up to 15 km from the vent (Figs. 4 and 5C). The ignimbrite successions reach a thickness of 20 m at the break of slope closest to the vent. The southern wall of the Taftan crater was destroyed during the last andesitic eruption in the late Pleistocene (Fig. 5D; Ghazban, 2002).

3.2. Hydrothermal deposits and fumarolic alteration

In the late Miocene, extensive hydrothermal alteration occurred in the TVC (Fig. 6). The alteration types are mostly phyllic, argillic, and advanced argillic, and are related to porphyry and epithermal mineralization such as at the Kharestan and Bidester porphyry–epithermal Cu-Au prospects in the northwest (Figs. 4 and 6) and the Siah Jangal epithermal Au deposit to the northeast of the TVC. Younger Pliocene argillic and Quaternary fumarolic alteration also occurs in several locations on the west, east, and southeast flanks of the Taftan volcano (Fig. 6), but no mineralization related to these alteration zones has been reported to date.

3.2.1. Kharestan and Bidester porphyry Cu prospects

The Kharestan and Bidester porphyry–epithermal Cu-Au deposits (6.10 ± 0.80 Ma, and ~4.3 Ma; see below) are hosted by late Miocene andesitic volcanic and subvolcanic rocks, and Eocene flysch (Fig. 7A,B). They appear to be exposed at relatively shallow levels, with the majority of outcropping alteration consisting of oxidized and argillized quartz-sericite-pyrite (phyllic) alteration in andesitic volcanic rocks. Pyrite (oxidized to jarosite) is widespread as disseminations and veinlets (Fig. 7C,D). Advanced argillic alteration with alunite (Fig. 7E,F) and zones of gold mineralization also occurs in strongly silicified zones and lithocaps at both deposits (Fig. 7G). The oxidized pyritic stockwork zones suggest the possibility of supergene Cu enrichment below surface, and large boulders consisting of secondary malachite and chalcocite impregnations in volcanic rocks were found in gully beds at Bidester (Fig. 7H).

Five diamond drillholes have been completed by National Iranian Copper Industries Company (NICICo) in the main region of phyllic alteration at Kharestan to a maximum depth of 500 m. Copper grades are reported to be very low near surface but gradually increase with depth to a maximum of ~0.15 % Cu in potasically altered volcanic and subvolcanic rocks. Due to the low grades of copper encountered drilling was not continued, and a resource has not been estimated; nevertheless, exploration continues on the prospect by Pars Tamin.

At Bidester, a large zone of gold mineralization in siliceous lithocap has been outlined by surface sampling, and limited diamond drilling has encountered short intervals of quartz diorite and quartz monzonite intruded into volcanic rocks, with potassic overprinted by phyllic alteration.

3.2.2. Siah Jangal epithermal Au deposit

The Siah Jangal epithermal Au deposit, located ~25 km northeast of the Taftan edifice, is related to Miocene dioritic to monzodioritic intrusions and is hosted by Mesozoic flysch. The main alteration zone (1.5 x 5 km) consist of intense argillic alteration in the intrusive and metasedimentary rocks, with locally abundant Fe-oxide staining along fractures. Gold grades of up to 8 ppm Au have been reported from seven trenches in zones of abundant Fe-oxide veins, which are likely an oxidation product of pyritic veinlets. A limited drilling program is currently underway on several gold-bearing siliceous veins in the Siah Jangal area.

3.2.3. Other alteration zones

A third large argillic to advanced argillic alteration zone, ~5 x 5 km, occurs ~10 km to the WNW of the Taftan volcano. This zone is aligned with the Kharestan and Bidester porphyry systems along an ESE trend, each spaced ~8 km apart (Figs. 6, 8A). No exploration has been conducted on this alteration zone, although it has the characteristics of a shallow-level epithermal system potentially overlying a porphyry system as at Kharestan and Bidester.

Fumarolic alteration locally affects the Quaternary volcanic rocks around the current Taftan edifice and at the summit, where active fumarolic vents emit sulfurous gases (Figs. 6, 8B). Ghazban (2002) reported that these altered rocks mainly consist of alunite, kaolinite, and residual silica.

4. Sampling

Forty-six samples of fresh volcanic and plutonic rocks from the Taftan Volcanic Complex were collected from surface outcrops during two field seasons in August 2012 and July 2013. All surface weathering was removed by hammering in the field, and hand specimens were sent for polished section preparation to ZarAzma laboratory in Tehran. Large (multi-kg) samples were collected in the field, but much of this material was lost in shipping. Most analyses are therefore based on smaller (~1 kg) hand samples that were shipped separately. Although this sample size is less than ideal, the relatively fine grain size of most of the

volcanic rocks means that these samples should be representative of the bulk rock composition (an assumption supported by the relatively tight grouping of analytical results; see §9).

In addition to the samples from Taftan, ten samples of andesitic to dacitic lava were collected from the Bazman volcano for comparison purposes.

Locations of all analyzed samples, along with field descriptions and whole-rock analytical data are listed in Appendix A.

5. Analytical techniques

5.1. $^{40}Ar/^{39}Ar$ geochronology

Biotite and amphibole from unaltered rocks from the Taftan and Bazman volcanic complexes were prepared for $^{40}Ar/^{39}Ar$ dating at the University of Alberta. After petrographic study, those samples that had unaltered amphibole and biotite were crushed and sieved; heavy minerals in the 0.5–1 mm fraction were separated by density using bromoform liquid, and whole biotite and amphibole crystals or cleavage fragments were hand-picked under a binocular microscope. Two samples of alunite from the Kharestan and Bidester porphyry-epithermal prospects were also prepared by hand-picking crystals from lightly crushed rock samples.

Mineral aliquots were analyzed in the Nevada Isotope Geochronology Laboratory at the University of Nevada, Las Vegas. Details of analytical methods are listed in Appendix B. Geochronological results are reported to ±1σ in Appendix D, but ages are reported to ±2σ.

5.2. Electron microprobe analysis and data reduction

The compositions of amphibole, orthopyroxene, and clinopyroxene phenocrysts, and Fe-Ti oxide microphenocrysts in 14 polished thin sections of volcanic rocks from the Taftan and Bazman volcanic complexes were analyzed by wavelength dispersive spectrometry (WDS), using a JEOL JXA-8900R electron microprobe at the University of Alberta, operated with a 15 nA beam current, 15 kV accelerating potential, and 1 μm beam diameter for all minerals. Total count times of 30 seconds were used for both peaks and backgrounds for all elements except F (40 s). The X-ray lines and analyzing crystals were: F *K*α, LDE1; Na *K*α, TAP; K *K*α, PET; Si *K*α, TAP; Fe *K*α, LiF; Mg *K*α, TAP; Ca *K*α, PET; Al *K*α, TAP; Mn *K*α, LiF; Cl *K*α, PET; Ti *K*α, PET; Cr *K*α, LiF. The reference standards consisted of metals, synthetic inorganic materials, and natural minerals (Jarosewich et al., 1980). Corrections were applied

to F for interference by Fe. Oxygen was calculated by cation stoichiometry and included in the matrix correction. The X-ray intensity data were reduced following Armstrong (1995).

Detection limits were typically lower than 300 ppm for major elements and 1300 ppm for fluorine. Full data are listed in Appendix C.

Formulas for the amphiboles were calculated following the IMA 2012 guidelines (Hawthorne et al., 2012) using the spreadsheet of Locock (2014). The formulas for the pyroxenes and oxides were calculated on the basis of stoichiometry following Droop (1987).

Based on the recommendations of Erdmann et al. (2014), crystallization temperatures and log fO_2 values were calculated for the mean amphibole data using the expressions of Ridolfi et al. (2010); pressures and melt-H_2O contents derived from these expressions are not considered reliable (Erdmann et al., 2014). The more recent work of Putirka (2016) yields very similar temperatures.

For the oxides, the ILMAT spreadsheet (Lepage, 2003) was used with the mean data for magnetite–ilmenite pairs to calculate crystallization temperature and fO_2. The latter parameter is expressed in log units with respect to the fayalite-magnetite-quartz (ΔFMQ) buffer calculated at 1 kbar following Frost (1991).

In contrast to the amphiboles, the oxide data fall into two T–log fO_2 populations, likely reflecting re-equilibration of some of the oxide pairs (Frost and Chacko, 1989; Frost and Lindsley, 1991).

5.3. Whole rock geochemistry

Seventeen samples from the TVC and four samples from the Bazman volcano were prepared for geochemical analysis in two stages. Samples collected in 2012 were prepared at ZarAzma laboratory (Tehran, Iran) by crushing and grinding in a steel mill, whereas samples collected in 2013 were shipped directly to Canada and were prepared by crushing (mostly by jaw crusher, but some samples were crushed by hammer) and grinding in a steel ring mill (SPEX 8500 Shatterbox®) at the University of Alberta. All powdered samples were sent to Activation Laboratories (Ancaster, Ontario, Canada) for analysis.

A combination of fusion inductively-coupled-plasma mass spectrometry (ICP-MS) and instrumental neutron activation analysis (INAA) was used (Actlabs 4E-Research analytical package with ICP-MS). For each sample, a 0.2 gram split of milled powder was fused with a lithium metaborate/lithium tetraborate mixture, and was then digested in 5% HNO_3 followed by ICP-MS analysis. For INAA, one gram aliquots were irradiated at a thermal neutron flux

of 7×10^{12} n cm^{-2} s^{-1} for a week prior to gamma ray analysis. Limits of detection for major elements were 0.01 wt.%, except MnO and TiO_2, which were 0.001 wt.%. Trace elements generally have detection limits less than 1 ppm. Accuracy for major elements, as determined by reproducibility of standards and duplicates, is typically within 5 relative % (< 3 relative % for SiO_2 and Al_2O_3), and to within 10 relative % for minor and trace elements.

6. $^{40}Ar/^{39}Ar$ geochronological results

The results of $^{40}Ar/^{39}Ar$ analyses of four biotite and one amphibole mineral separates from volcanic rocks from the Taftan area and two samples of alunite from the Kharestan and Bidester porphyry-epithermal deposits are summarized in Table 1 and illustrated in Figure 9; full data are listed in Appendix D. The Kharestan alunite sample (12AR010) yielded a statistically valid plateau age of 6.10 ± 0.80 Ma (±2 s.d.), in 5 steps containing 79% of the ^{36}Ar release (Fig. 9A). The Bidester alunite sample (BID-1) did not yield a statistically reliable plateau age (Fig. 9B), but steps 3–8 (85% of the ^{39}Ar released) yielded a weighted mean age of 4.34 ± 0.02 Ma (compared with a total gas age of 4.95 ± 0.06 Ma). Four biotite samples from volcanic rocks yielded generally undisturbed age spectra, with plateau ages ranging from 7.87 ± 0.14 Ma to 1.00 ± 0.08 Ma (Fig. 9C–F), consistent with the positions of the samples within the stratigraphy.

One amphibole sample from a pumice fragment in a Quaternary ignimbrite (sample 13AR017) did not yield a plateau age (Fig. 9G). Early steps yielded ages up to ~7 Ma, whereas the last eight steps (77% of the ^{39}Ar released) yielded a weighted mean age of 404 ± 82 ka (see Appendix D). The older apparent ages in early steps may be due to the presence of excess ^{40}Ar. Although no plateau age was achieved for this sample, the weighted mean age from the later steps suggests a late Pleistocene age (~0.4 Ma) for this ignimbrite. These new $^{40}Ar/^{39}Ar$ ages from Taftan are in broad agreement with U-Pb zircon ages of 3.4 to 0.8 Ma reported by Pang et al. (2014).

A single amphibole sample from an dacitic clast in a block-and-ash flow from the Bazman volcano (sample 12AR029) did not yield a plateau age (Fig. 9H), but returned a total gas age of 1.9 ± 0.3 Ma.

7. Petrography of volcanic rocks from the Taftan Volcanic Complex

Polished thin sections of all collected samples were studied using a petrographic microscope to determine mineralogy and texture, and are described below in terms of the six spatio-temporal groups mapped in Figure 4.

7.1. Group 1: Late Miocene andesitic and dacitic lava flows

Voluminous andesite–dacite lava flows form the oldest phase of Taftan volcanism, and cover the western part of the TVC. The lavas are fairly uniform in composition and texture but in some localities show flow banding. A representative sample of andesite (sample 12AR017) yielded a plateau age of 7.87 ± 0.14 Ma.

Phenocrysts consist of plagioclase, amphibole, and orthopyroxene, with less abundant microphenocrysts of magnetite and ilmenite. Plagioclase crystals are mostly fresh but commonly show oxidized rims (opacitization); some magnetite grains are also partially oxidized to hematite. The groundmass is typically partially devitrified (spherulitic), and includes fine-grained plagioclase microcrystals (Fig. 10A).

7.2. Groups 2-5: Plio-Pleistocene andesite and dacite lava flows

Four map units of andesitic to dacitic lava flows and tuffs are recognized in the eastern part of the TVC (Fig. 4). These units consist of late Pliocene andesitic to dacitic lava flows (groups 2 and 3: samples 13AR006, 3.10 ± 0.06 Ma, and 13AR008, 2.67 ± 0.08 Ma), Pleistocene andesitic to dacitic lava flows (group 4), and Pleistocene andesitic ignimbrite (group 5: sample 13AR016: 1.00 ± 0.08 Ma). Around the current Taftan crater, the primary morphology of the lavas is well preserved. Flow banding is commonly present in the Quaternary andesite and dacite lavas on the northern side of the volcano (group 3). Major phenocryst phases in andesites are amphibole, plagioclase, orthopyroxene, and clinopyroxene with minor magnetite and ilmenite. Dacite samples contain amphibole, plagioclase, and orthopyroxene phenocrysts, with less abundant biotite, quartz, rutile, titanite, magnetite, and ilmenite. Most of the plagioclase microphenocrysts are fresh but some grains are spotted by sericite; they show oscillatory zoning and sieve textures (Fig. 10B). Embayments are commonly observed in quartz phenocrysts (Fig. 10C). Ferromagnesian minerals (amphibole, biotite, and pyroxene) are mostly fresh, but some grains are partially to completely opacitized (Fig. 10C,D). The matrix is typically fine-grained to glassy, variably devitrified, and locally vesicular. The glassy groundmass is normally colorless in thin section, but in some samples

light-brown to dark-brown glass occurs interstitially. Lath-shaped plagioclase and amphibole crystallites occur in the matrix.

Some mafic enclaves are also observed in dacitic rocks on the east and southeast sides of the Taftan volcano. The enclaves mainly consist of clusters of amphibole (commonly opacitized; Fig. 10E), plagioclase, and minor orthopyroxene, suggesting derivation from earlier crystallized magma below the volcano.

7.3. Group 6: Quaternary ignimbrite

Poorly welded ignimbrites (sillars) are the youngest volcanic units in the map area (group 6, Fig. 4; sample 13AR017: ~0.5 Ma). The ignimbrite deposits mainly occur on shallow slopes of the distal eastern and southeastern flanks of the Taftan volcano. They are composed of andesitic tuff with lithic fragments that include clasts of andesite, dacite, and pumice (up to a few decimeters in diameter), and greenschist fragments from the underlying basement (Emami, 2000). The ignimbrite deposits probably reach thicknesses of ~20 m in valley fills close to the foot of the volcano, and directly overlie Eocene flysch deposits. They are well exposed in the walls of gullies and valleys that have been cut into the relatively soft deposits (Fig. 5C).

The glassy ignimbrite matrix contains phenocrysts of plagioclase, amphibole, pyroxene (orthopyroxene is dominant), and biotite, with microphenocrysts of magnetite and ilmenite. Plagioclase phenocrysts are subhedral and show oscillatory zoning. The ashy matrix is partially welded and vesicles are common. Flattened and stretched pumice clasts (fiammé) are also abundant, indicating some compaction and secondary mass flow of the ignimbrite after deposition (Cas and Wright, 1991; Fig. 10F).

8. Mineralogy of volcanic rocks from the Taftan Volcanic Complex

8.1. Pyroxenes

Orthopyroxene is abundant in all rock samples from andesite to dacite, whereas clinopyroxene is rare. Average analyses of both types of pyroxene are listed in Table 2, and the full data are listed in Appendix C. Pyroxene phenocrysts mostly occur in glomeroporphyritic clusters with plagioclase and rarely with olivine. The Mg# ($100MgO/(FeO + MgO + MnO + Fe_2O_3)$ on a molar basis) of orthopyroxene phenocrysts ranges from 63.2 to 74.5 (average = 66.6 ± 1.9, n = 45), whereas two clinopyroxene analyses yielded values of 68.6 and 78.9.

8.2. Magnetite and ilmenite

Magnetite is the most abundant opaque mineral phase in andesitic and dacitic rocks (Fig. 11A); average analyses are listed in Table 3, and full data are listed in Appendix C. Crystals are typically smaller than 200 μm and occur as either individual microphenocrysts in the groundmass or as inclusions within ferromagnesian silicate phases. Martitization locally occurs in some samples, and those samples were excluded from analysis.

Minor ilmenite also occurs in most rock samples as small (<100 μm) lath-shaped crystals in the groundmass, as exsolution lamellae in magnetite, or as equilibrium intergrowths with magnetite grains (Fig. 11A).

8.3. Amphiboles

Amphibole phenocrysts in the Taftan volcanic rocks typically occur as euhedral to subhedral crystals, 0.2 to 5 mm in length. However, crystals larger than 10 mm were also observed in some andesite samples (e.g., 12AR018 and 13AR013). Most amphibole phenocrysts in the Taftan volcanic rocks contain small plagioclase and apatite inclusions (Fig. 11B). Many crystals also show oxidation reactions in which amphibole rims are replaced by "opacite" (fine-grained Fe-Ti oxide intergrowths; Fig. 11C). Oxidation of amphiboles in andesite samples is typically incomplete and opacitized rims were not observed to exceed a thickness of 100 μm, but in many dacite samples some of the amphibole phenocrysts are totally opacitized (Fig. 11D). This texture can be attributed either to oxidation or depressurization during magma ascent (Rutherford and Hill, 1993; Chambefort et al., 2013).

The compositions of amphibole phenocrysts from the TVC are presented in Table 4 (full data are listed in Appendix C). All the amphiboles analyzed are calcic and are mostly magnesio-hastingsite (the ferric analogue of pargasite; Fig. 12).

9. Geochemistry of volcanic rocks

Whole-rock geochemical data for samples from the TVC and Bazman volcano are listed in Appendix A. For petrological classification purposes, major element compositions were normalized to 100% volatile free. Most samples had low loss-on-ignition (LOI) contents (<1.5 wt.%) except for five samples from the older Miocene sequences in the western part of the TVC that had LOI between 2.4-8.7 wt.%; these samples show evidence of devitrification

and hydration of glassy matrices rather than hydrothermal alteration, and are therefore included in the petrological discussion. Volcanic rock samples are classified based on the IUGS definition of total alkalis versus silica (TAS; Le Maitre, 2002), and are illustrated in Figure 13A.

9.1. Major elements

All volcanic rock samples collected from Taftan and Bazman are intermediate to felsic in composition with SiO_2 contents ranging from 57.6 wt.% to 69.1 wt.% (normalized to 100% volatile free), and metaluminous. All samples are subalkaline and plot in the calc-alkaline to high-K calc-alkaline fields (Fig. 13B). The samples from Bazman are mostly calc-alkaline dacites, with distinctly lower K_2O contents than the Taftan dacites, whereas the Taftan samples straddle the high-K calc-alkaline / calc-alkaline boundary, with slightly more potassic compositions in two of the older Miocene rocks. The chemical variations of major and minor elements Al_2O_3, MgO, TiO_2, Na_2O, K_2O, and P_2O_5 relative to SiO_2 are shown in Figure 14. Although this is not a single coeval fractionation suite (spanning ~8 m.y. and two locations) the samples show fairly coherent inverse trends for most major elements relative to SiO_2, likely reflecting fractionation of ferromagnesian minerals such as pyroxene and amphibole; Al_2O_3, Na_2O, and K_2O tend to increase with SiO_2, likely reflecting relatively late crystallization and fractionation of feldspars. The Taftan and Bazman suites are generally similar, and only the older (Miocene) rocks from the TVC show slightly lower Al_2O_3 and Na_2O, and higher K_2O and CaO than the other samples.

9.2. Trace elements

Primitive mantle-normalized trace element and chondrite-normalized rare earth element diagrams for samples of the TVC and Bazman are shown in Figures 15 and 16 (normalization values from Sun and McDonough, 1989). All samples show relative depletions in Nb, Ta, and Ti and enrichments in incompatible elements, which are characteristic signatures of continental volcanic arc rocks (Gill, 1981; Pearce and Peate, 1995). Strong depletions of Ti and P in dacitic rocks are enhanced by fractionation of magnetite, amphibole, and apatite. Enrichments in incompatible elements such as Rb, Ba, Th, and U likely reflect a combination of source enrichment and fractionation processes (see discussion below). The TVC suite is distinctly more enriched in incompatible elements than the Bazman samples, consistent with the slightly less potassic character of the latter suite.

The samples show moderate enrichments of light rare earth elements (LREE) relative to middle and heavy rare earth elements (MREE and HREE) with listric-shaped patterns on chondrite-normalized diagrams lacking negative Eu anomalies (Fig. 16). Such patterns reflect abundant early amphibole crystallization with minimal or delayed plagioclase fractionation, characteristic of hydrous intermediate-composition magmas (Frey et al., 1978; Hanson, 1980; Lang and Titley, 1998; Müntener and Ulmer, 2006). The TVC samples show slightly greater enrichments in LREE compared to the Bazman suite.

10. Estimates of magmatic temperature and redox conditions

Analyses of coexisting magnetite-ilmenite mineral pairs and amphibole compositions are used to provide constraints on temperature and redox state of the evolving magmas, based on the formulations of Andersen and Lindsley (1985) and Ridolfi et al. (2010). We did not attempt to calculate pressure and magmatic water contents from amphibole compositions using the equations of Ridolfi et al. (2010) because these values are thought to be unreliable (Erdmann et al., 2014). However, the widespread presence of amphibole phenocrysts in both andesitic and dacitic rocks from the Bazman and Taftan volcanoes indicates water contents >4 wt.% (Naney, 1983; Merzbacher and Eggler, 1984; Rutherford and Devine, 1988).

10.1. Magnetite-ilmenite pairs

The results of magnetite-ilmenite thermometry and oxybarometry for six samples of andesite from the Taftan and Bazman volcanoes are summarized in Table 5 and illustrated in Figure 17. No suitable equilibrated magnetite-ilmenite pairs were found in dacitic rock samples. The ILMAT Excel spreadsheet (Lepage, 2003) was used to estimate temperature and oxygen fugacity (fO_2). The uncertainty for temperature and fO_2 are estimated to be at best ±35°C and ±0.2 log fO_2 units (Spencer and Lindsley, 1981). The crystal pairs used for calculation had Mg/Mn ratios consistent with equilibrium between melt and minerals, as defined by Bacon and Hirschmann (1988). Twelve representative magnetite–ilmenite pairs from six andesitic rocks yielded temperatures from 734°C to 924°C, and redox states (relative to the fayalite-magnetite-quartz buffer, ΔFMQ) ranging from +1.0 to +3.8. However, there is distinct bimodality in the temperature data between mineral pairs equilibrated ~900°C and those below ~850°C. The lower temperatures are interpreted to reflect subsolidus re-equilibration (Frost and Chacko, 1989; Frost and Lindsley, 1991), as indicated by evidence for partial oxidation and exsolution in some magnetite samples. Accepting only the higher-

temperature pairs as reflective of magmatic conditions yields an average temperature of 882° ± 26°C and ΔFMQ = 2.0 ± 0.1 for the Taftan and Bazman andesites.

10.2. Amphibole

The crystallization temperature and oxygen fugacity (fO_2) during crystallization of amphibole phenocrysts from eleven samples of andesitic and dacitic rocks from the Taftan and Bazman volcanoes were estimated from electron microprobe analyses using the method of Ridolfi et al. (2010) (Table 5, Fig. 17). This thermometer is valid for temperatures between 550°–1120°C. The uncertainties for temperature and fO_2 are estimated to be at best ±25°C and ±0.4 log fO_2 (Ridolfi et al., 2010).

Crystallization temperature ranges from 859° to 1026°C, and oxidation state ranges from ΔFMQ = 1.2 to 2.2. When plotted against whole-rock SiO_2 content (for samples for which whole-rock analyses are available), crystallization temperature shows a steady decrease from ~1000°C to ~900°C, and oxidation state a small but steady increase from ΔFMQ ~1 to ~2 with fractionation (as represented by silica content; Fig. 18). Although this is not a comagmatic suite (including samples from both Taftan and Bazman, and rocks of slightly different ages), the data trends are consistent with expected changes in temperature and oxidation state during crystallization and degassing (e.g., Mathez, 1984; Candela, 1986; Bell and Simon, 2011; Richards et al., 2013).

11. Discussion

11.1. TVC and Bazman magma evolution

Magma source processes can be reconstructed from primitive mafic magmas, but they can be hard to reconstruct for intermediate to felsic magmas due to mineral fractionation and contamination processes that likely occur during magma ascent through the upper crust (Davidson, 1996; Davidson et al., 2005). The TVC magmas show LILE enrichment as well as Ta, Nb, and Ti depletions, which are characteristic signatures of subduction-related arc magmas. Additionally, $^{143}Nd/^{144}Nd$ and $^{87}Sr/^{86}Sr$ isotopic ratios of the Taftan volcanic rocks (data from Pang et al., 2014) indicate evolution of the TVC from arc-related magma, with some degree of crustal involvement. A qualitative assessment of crustal magmatic processes in the TVC volcanic suite is presented below using major element trends and variations of trace element ratios.

On Harker diagrams, depletion of MgO, (FeO, not shown), CaO, TiO_2, and P_2O_5 versus SiO_2 (Fig. 14) suggest fractionation of ferro-magnesian mineral phases such as pyroxene and amphibole, Fe-Ti oxides such as magnetite, and apatite. Alkalis (Na_2O and K_2O) and Al_2O_3 show increasing or scattered trends with SiO_2, consistent with late fractionation of alkali-rich aluminous minerals such as sodic plagioclase and biotite (K-feldspar was not observed as a phenocryst phase in these rocks).

On a plot of Sr/Y vs. La/Yb (Fig. 19), the Taftan samples plot at generally higher Sr/Y and La/Yb ratios than the Bazman suite, reflected also in the steeper and more listric shaped REE patterns of the Taftan samples compared to Bazman (Fig. 16). Ratios of Sr/Y and La/Yb > 20 in intermediate composition rocks are sometimes described as adakitic, with high values reflecting restitic or fractionating garnet in the absence of early fractionating plagioclase. However, in this case, the slightly elevated Sr/Y and La/Yb ratios, listric REE profiles, and lack of Eu anomalies almost certainly reflect fractionation of amphibole (and delayed plagioclase fractionation) from hydrous magmas, which has been linked to magma fertility for the formation of porphyry Cu deposits (Richards and Kerrich, 2007; Richards, 2011; Chiaradia et al., 2012; Richards et al., 2012; Loucks, 2014). The data suggest that the Taftan magmas were distinctly more hydrous than Bazman, an observation consistent with the presence of at least two porphyry deposits in the TVC but none known at Bazman.

11.2. Comparison of the TVC and Bazman suites with the Kerman and Chagai Belts

Shafiei et al. (2009) reported geochemical data for largely barren pre-collisional (Paleogene: "Jebal Barez-type") and fertile post-collisional (Neogene: "Kuh Panj-type") igneous rocks from the Kerman Belt. These authors described the Paleogene Jebal Barez suite as plagioclase-quartz-K-feldspar granitoids with minor ferromagnesian minerals, and relatively low Sr/Y and La/Yb ratios. In contrast, the mineralized Neogene Kuh Panj granitoids are mostly plagioclase-quartz-amphibole-phyric, with higher Sr/Y and La/Yb ratios. Similarly, Siddiqui (2004) and Richards et al. (2012) reported geochemical data for Paleogene and Neogene igneous rocks from the Chagai Arc in Pakistan. The largely barren Paleogene volcanic rocks are mostly pyroxene-plagioclase volcanic rocks with low Sr/Y and La/Yb ratios, whereas Neogene rocks associated with the Reko Diq and Saindak porphyry deposits are pyroxene-amphibole-plagioclase-phyric with higher Sr/Y and La/Yb ratios. The range of data from the fertile Neogene magmas from both of these areas are plotted on Figures 15, 16, and 18, where it can be seen that the TVC samples broadly overlap the range

of fertile rocks from the Kerman Belt and Chagai Arc, and in particular share the same elevated Sr/Y and La/Yb ratios. In contrast, while the Bazman suite also largely overlaps the fertile suite ranges in Figures 15 and 16, the data plot at lower values for Sr/Y and La/Yb, and overlap the lower range for the Paleogene Jebal Barez suite (Fig. 19). As noted above, these results are consistent with the presence of porphyry-type mineralization within the TVC, but apparent lack at Bazman.

It is interesting to note the high degree of similarity in chemical composition between the Miocene rocks from the Kerman Belt, the TVC, and the Neogene Chagai Belt. While the TVC, Bazman, and Chagai Belt magmas are thought to be related to active subduction, Shafiei et al. (2009) have argued that the Miocene Kerman Belt rocks are related to post-collisional magmatic processes. The timing of Afro-Arabian–Eurasian collision is widely debated (see reviews by Richards, 2015, and Richards and Sholeh, 2016), the consensus view is that collision along the Iranian section of the orogen occurred in the late Oligocene or earliest Miocene (e.g., Gholami Zadeh et al., 2017), placing the mid-Miocene (12–11 Ma) porphyry-related Kuh Panj magmatism in a late or post-collisional setting.

Syn- or post-collisional models for high-Sr/Y calc-alkaline magmatism and porphyry formation invoke partial melting of previously subduction modified lithosphere (e.g., lower crustal arc cumulates and/or subduction metasomatized subcontinental lithospheric mantle; Hou et al., 2009; Richards, 2009; Shafiei et al., 2009). As has been noted by these and subsequent authors, and reaffirmed here, it is remarkable how similar these collision-related magmas and porphyry systems are to normal subduction-related high-K calc-alkaline suites and deposits. No geochemical or isotopic indicators have yet been identified that distinguish clearly between magmas and porphyry deposits formed in these distinct tectonic settings, and indeed for many years the Kerman suite magmas and deposits were assumed to reflect subduction; the realization that they are collision-related has only come from a more precise understanding of the timing of collision along the orogen.

The similarity between subduction-related and collisional high-K calc-alkaline magmas can be interpreted to indicate that their chemistry is largely controlled by processes within the upper plate lithosphere, albeit with an ultimate source in the asthenospheric mantle wedge. In the case of collisional magmas, the direct source rock is previously subduction-modified lithosphere (metasomatized subcontinental lithospheric mantle and/or lower crustal arc cumulates), partial melting of which will yield magmas with similar chemical and isotopic compositions to the original arc magmas. In some cases, these collision-related magmas can

be enriched in Au and platinum group elements, but in the case of the Kerman Belt (and Gangdese Belt, Tibet; Hou et al., 2009) the related porphyry deposits are simply enriched in Cu±Mo, as for normal subduction-related porphyries.

11.3. Porphyry–epithermal potential of the Taftan volcanic complex

Hydrous (>4 wt.% H_2O) and relatively oxidized (up to ΔFMQ+2) arc magmas can generate magmatic hydrothermal Cu±Mo±Au ore deposits by exsolution of hydrothermal fluids from upper crustal magma chambers (Burnham, 1979; Richards, 2003, 2011; Cooke et al., 2005; Sillitoe, 2010).

The data presented above suggest that volcanic rocks of the Taftan and Bazman volcanic complexes are products of magmatism in the Makran Arc in response to subduction of Indian Oceanic lithosphere beneath Central Iran. The long-lived magmatic activity of the TVC, since the late Miocene to the Pleistocene, suggests that a large volume of magma has been active in the mid- to upper crust for ~8 m.y. The TVC magmas were hydrous (as indicated by abundant amphibole phenocrysts) and relatively oxidized (ΔFMQ = +1 to +2), and were fertile for the formation of magmatic-hydrothermal ore deposits, as indicated by the presence of the Kharestan (6.1 ± 0.4 Ma) and Bidester (~4.3 Ma) porphyry–epithermal Cu-Au deposits, the Siah Jangal epithermal Au prospect, and large argillic to advanced argillic alteration zones that may host epithermal mineralization.

12. Conclusions

The large (~20 km diameter) Taftan volcanic complex was formed by multiple eruptions of volcanic materials over a period of ~8 m.y. from the late Miocene to the Quaternary. The earliest volcanic activity started with eruption of andesitic to dacitic lava flows on the Cretaceous to Eocene volcanic and sedimentary paleosurface. In the Pliocene, the Taftan magmatic center shifted 20 km ESE to its current location, and has erupted voluminous andesitic and dacitic lavas and pyroclastic materials since ~3.1 Ma.

Major and trace element compositions of the Taftan rocks show that they are typical of subduction-related calc-alkaline to high-K calc-alkaline magmas, with depletions of Nb, Ta, and Ti and relative enrichments of LILE and Th and U. In comparison, the Bazman rocks are somewhat less enriched in incompatible elements, and are mostly calc-alkaline in composition.

The geochemical signatures of the TVC magmas indicate that they originated in the mantle wedge and evolved by fractional crystallization of olivine, pyroxene, and amphibole, with delayed plagioclase crystallization due to relatively high magmatic water contents. Lower Sr/Y and La/Yb ratios in the Bazman suite suggest lower magmatic water contents.

These differences, and the trace element similarities between the TVC and fertile Miocene rocks from the Kerman and Chagai Belts, are consistent with the observation that the TVC hosts at least two porphyry Cu deposits and several epithermal systems, whereas the Bazman volcano appears to be largely barren for porphyry mineralization.

Regionally, the geochemical similarity between porphyry-related magmas from the collisional Kuh Panj suite, and the subduction-related TVC and Chagai Belt are remarkable, and provide no clear discrimination between these distinct tectonic settings.

Acknowledgements

This research was supported by a Discovery Grant from the Natural Sciences and Engineering Research Council of Canada to JPR (RGPIN 203099 and RGPIN-2017-05082). We additionally thank the National Iranian Copper Co (especially Messrs. Esfahanipour, Taghizadeh, and Khorasani) and IMIDRO Company (especially Messrs. Asgharzadeh, Shirkhani, and Fattahi) for financial, logistic, and accommodation support in the field, and for providing access to their properties throughout this project.

Mark Labbe and Martin von Dollen are thanked for sample preparation at the University of Alberta, and Mr. Shakourian for sample preparation at Zarazma Laboratory in Tehran. We thank John Menzies and an anonymous reviewer for constructive comments that have improved the manuscript.

References:

Ahmadzadeh, G., Jahangiri, A., Lentz, D., and Mojtahedi, M., 2010, Petrogenesis of Plio-Quaternary post-collisional ultrapotassic volcanism in NW of Marand, NW Iran: Journal of Asian Earth Sciences, v. 39, p. 37–50.

Allen, M.B., Kheirkhah, M., Neill, I., Emami, M.H., and Mcleod, C.L., 2013, Generation of arc and within-plate chemical signatures in collision zone magmatism: Quaternary lavas from Kurdistan Province, Iran: Journal of Petrology, v. 54, p. 887–911.

Andersen, D.J., and Lindsley, D.H., 1985, New models for the Ti-magnetite/ilmenite geothermometer and oxygen barometer: Abstract AGU 1985 Spring Meeting Eos Transactions, v. 46, p. 416.

Armstrong, J.T., 1995, CITZAF: a package of correction programs for the quantitative electron microbeam X-ray analysis of thick polished materials, thin-films, and particles: Microbeam Analysis, v. 4, p. 177-200.

Arshadi, S., and Förster H., 1983, Geological Structure And Ophiolites Of The Iranian Makran. Geodynamic Project (Geotraverse) In Iran (Final Report), Geological Survey Of Iran, Report No. 51, p. 479–88.

Aubourg, C., Smith, B., Bakhtari, H., Guya, N., Eshraghi, A., S., L., Molinaro, M., Braud, X., Delaunay, S., 2004, Post-Miocene shortening pictured by magnetic fabric across the Zagros-Makran syntaxis. In "Orogenic curvature: integrating paleomagnetic and structural analyses." (A. J. Sussman, and A. B. Weil, Eds.), pp. 17-40. Geological Society of America special paper, Boulder, Colorado.

Bacon, C.R., and Hirschmann, M.M., 1988. Mg/Mn partitioning as a test for equilibrium between coexisting Fe–Ti oxides: American Mineralogist, v. 73, p. 57–61.

Bayer, R., Chery, J., Tatar, M., Vernant, P., Abbassi, M., Masson, F., Nilforoushan, F., Doerflinger, E., Regard, V., and Bellier, O., 2006, Active deformation in Zagros-Makran transition zone inferred from GPS measurements: Geophysical Journal International, v. 165, p. 373–381.

Bell, A.S., and Simon, A., 2011, Experimental evidence for the alteration of the $Fe^{3+}/\Sigma Fe$ of silicate melt caused by the degassing of chlorine-bearing aqueous volatiles: Geology, v. 39, p. 499–502.

Berberian F., and Berberian, M., 1981, Tectono-plutonic episode in Iran. Geodynamic series, 3, WG6, American Geophysical Union, 5-32.

Biabangard, H., and Moradian, A., 2008, Geology and geochemical evaluation of Taftan Volcano, Sistan and Baluchestan Province, Southeast of Iran: Chinese Journal of Geochemistry, v. 27, p. 356–369.

Burnham, C.W., 1979, Magmas and hydrothermal fluids, in Barnes, H.L., ed., Geochemistry of hydrothermal ore deposits, 2nd edition: New York, John Wiley and Sons, p. 71–136.

Byrne, D.E., Sykes, L.R., and Davis, D.M., 1992, Great thrust earthquakes and aseismic slip along the plate boundary of the Makran Subduction Zone: Journal of Geophysical Research, v. 97, p. 449-478.

Candela, P.A., 1986, The evolution of aqueous vapor from silicate melts: Effect on oxygen fugacity: Geochimica et Cosmochimica Acta, v. 50, p. 1205–1211.

Cas, R.A.F., and Wright, J.V., 1991, Subaquoeus Pyroclastic Flows And Ignimbrites: An Assessment: Bulletin Of Volcanology, v. 53, p. 357-380.

Chambefort, I., Dilles, J.H., and Longo, A., 2013, Amphibole geochemistry of the Yanacocha Volcanics, Peru: evidence for diverse sources of magmatic volatiles related to gold ores: Journal of Petrology, v. 54, p. 1017–1046, doi: 10.1093/petrology/egt004.

Chiaradia, M., Ulianov, A., Kouzmanov, K., and Beate, B., 2012, Why large porphyry Cu deposits like high Sr/Y magmas? Scientific Reports, v. 2, 685; DOI: 10.1038/srep00685

Cooke, D.R., Hollings, P., and Walshe, J.L., 2005, Giant porphyry deposits: characteristics, distribution, and tectonic controls: Economic Geology, v. 100, p. 801–818.

Davidson, J.P., 1996, Deciphering mantle and crustal signatures in subduction zone magmatism, *in* Bebout, G.E., Scholl, D.W., Kirby, S.H., and Platt, J.P., eds., Subduction: Top to bottom: American Geophysical Union, Geophysical Monograph 96, p. 251–262.

Davidson, J., Hassanzadeh, J., Berzins, R., Stockli, D.F., Bashukooh, B., Turrin, B., and Pandamouz, A., 2004, The geology of Damavand volcano, Alborz Mountains, northern Iran: Geological Society of America Bulletin, v. 116, p. 16–29.

Davidson, J.P., Hora, J.M., Garrison, J.M., and Dungan, M.A., 2005, Crustal forensics in arc magmas: Journal of Volcanology and Geothermal Research, v. 140, p. 157–170.

Droop, G.T.R., 1987, A general equation for estimating Fe^{3+} concentrations in ferromagnesian silicates and oxides from microprobe analyses, using stoichiometric criteria. Mineralogical Magazine, v. 51, p. 431–435.

Ellouz-Zimmermann, N., Lallemant, S.J., Castilla, R., Mouchot, N., Leturmy, P., Battani, A., Buret, C., Cherel, L., Desaubliaux, G., Deville, E., Ferrand, J., Lügcke, A., Mahieux, G., Mascle, G., Mühr, P., Pierson-Wickmann, A.-C., Robion, P., Schmitz, J., Danish, M.,

Hasany, S., Shahzad, A., and Tabreez, A., 2007, Offshore frontal part of the Makran accretionary prism: the Chamak survey (Pakistan), *in* Lacombe, O., Lavé, J., Roure, F., and Verges, J., eds., Thrust Belts and Foreland Basins: Springer, Berlin, p. 351–366.

Emami, M.H., 2000, Magmatism In Iran. G.S.I, Isbn: 964-6178-01-4, 608 p.

Erdmann, S., Martel, C., Pichavant, M. and Kushnir, A., 2014, Amphibole as an archivist of magmatic crystallization conditions: problems, potential, and implications for inferring magma storage prior to the paroxysmal 2010 eruption of Mount Merapi, Indonesia: Contributions to Mineralogy and Petrology, v. 167, p. 1-23.

Falcon, N.L., 1974, Southern Iran: Zagros Mountains. In: Spencer, A. (Ed.) Mesozoic–Cenozoic Orogenic Belts: Geological Society, London, Special Publications, v. 4, p. 199–211.

Farhoudi, G., Karig, D.E., 1977, Makran of Iran and Pakistan as an active arc system: Geology, v. 5, p. 64-68.

Firouzkouhi, Z., Ahmadi, A., Lentz, D.R., and Moridi-Farimani, A.-A., 2017, Mixing of basaltic and andesitic magmas in the Bazman volcanic field of southeastern Iran as inferred from plagioclase zoning: Mineralogical Magazine, v. 81, p. 975-985.

Frey, F.A., Chappell, B.W., and Roy, S.D., 1978, Fractionation of rare-earth elements in the Tuolumne Intrusive Series, Sierra Nevada batholith, California: Geology, v. 6, p. 239–242.

Frost, B.R., 1991. Introduction to oxygen fugacity and its petrologic importance: Reviews in Mineralogy and Geochemistry, v. 25, p. 1-9.

Frost, B.R., and Chacko, T., 1989, The granulite uncertainty principle: limitations on thermobarometry in granulites: Journal of Geology, v. 97, 435-450.

Frost, B.R., and Lindsley, D.H., 1991, Occurrence of iron-titanium oxides in igneous rocks: Reviews in Mineralogy and Geochemistry, v. 25, 433–468.

Gansser, A., 1971, The Taftan volcano (SE Iran): Eclogae geologicae Helvetiae, v. 64, p. 319–334.

Geological Survey of Iran, 1984a, Nuk Abad 1:100,000 geological map sheet.

Geological Survey of Iran, 1984b, Taftan 1:100,000 geological map sheet.

Ghazban, F., 2002, Geological and geothermal investigation of Mount Taftan, SE Iran: Geothermal Resources Council Transactions, v. 26, p. 22-25.

Gholami Zadeh, P., Adabi, M.H., Hisada, K.-i., Hosseini-Barzi, M., Sadeghi, A., and Ghassemi, M.R., 2017, Revised version of the Cenozoic Collision along the Zagros

Orogen, Insights from Cr-spinel and Sandstone Modal Analyses: Scientific Reports, v. 7, 10828, doi:10.1038/s41598-017-11042-1

Gill, J.B., 1981, Orogenic andesites and plate tectonics: New York, Springer-Verlag, 390 p.

Grando, G., and McClay, K., 2007, Morphotectonics domains and structural styles in the Makran accretionary prism, offshore Iran: Sedimentary Geology, v. 196, p. 157–179.

Hanson, G.N., 1980, Rare earth elements in petrogenetic studies of igneous systems. Annual Review of Earth and Planetary Sciences, v. 8, p. 371–406.

Hawthorne, F.C., Oberti, R., Harlow, G.E., Maresch, W.V., Martin, R.F., Schumacher, J.C., and Welch, M.D., 2012. Nomenclature of the amphibole supergroup: American Mineralogist, v. 97, p. 2031-2048.

Hou, Z., Yang, Z., Qu, X., Meng, X., Li, Z., Beaudoin, G., Rui, Z., Gao, Y., and Zaw, K., 2009, The Miocene Gangdese porphyry copper belt generated during post-collisional extension in the Tibetan Orogen: Ore Geology Reviews, v. 36, p. 25–51.

Jacob, K.H., and Quittmeyer, R.L., 1979, The Makran region of Pakistan and Iran: trench–arc system with active plate subduction, *in* Farah, A., and De Jong, K.A. (eds.), Geodynamics of Pakistan: Geological Survey of Pakistan, Quetta, p. 305–317.

Jarosewich, E., Nelen, J.A., and Norberg, J.A., 1980. Reference samples for electron microprobe analysis: Geostandards and Geoanalytical Research, v. 4, p. 43-47.

Kheirkhah, M., Neill, I., Allen, M.B., and Ajdari, K., 2013, Small-volume melts of lithospheric mantle during continental collision: Late Cenozoic lavas of Mahabad, NW Iran: Journal of Asian Earth Sciences, v. 74, p. 37–49.

Kukowski, N., Schillhorn, T., Flueh, E.R., and Huhn, K., 2000, Newly identified strike-slip plate boundary in the northeastern Arabian Sea: Geology, v. 28, p. 355-358.

Lang, J.R., and Titley, S.R., 1998, Isotopic and geochemical characteristics of Laramide magmatic systems in Arizona and implications for the genesis of porphyry copper deposits: Economic Geology, v. 93, p. 138–170.

Lawrence, R.D., Nakata, S.H., and Khan, T., 1992, Chaman fault, Pakistan–Afghanistan. Ann. Tectonicae, 6, 196–223.

Le Maitre, R.W., ed., 2002, Igneous Rocks: A Classification and Glossary of Terms, 2nd Edition: Cambridge University Press, 256 p.

Lepage, L.D., 2003, ILMAT: an Excel worksheet for ilmenite–magnetite geothermometry and geobarometry: Computers and Geosciences, 29, 673–678.

Liotard, J.M. Dautria, J.M., Bosch, D., Condomines, M., Mehdizadeh, H., and Ritz, J.-F., 2008, Origin of the absarokite–banakite association of the Damavand volcano (Iran): trace elements and Sr, Nd, Pb isotope constraints: International Journal of Earth Sciences, v. 97, p. 89–102.

Locock, A.J., 2014, An Excel spreadsheet to classify chemical analyses of amphiboles following the IMA 2012 recommendations: Computer and Geosciences, 62, 1-11.

Loucks, R.R., 2014, Distinctive composition of copper-ore-forming arc magmas: Australian Journal of Earth Sciences, v. 61, p. 5–16.

Mathez, E.A., 1984, Influence of degassing on oxidation-states of basaltic magmas: Nature, v. 310, p. 371–375.

McCall, G.J.H., 1997, The geotectonic history of the Makran and adjacent areas of southern Iran: Journal of Southeast Asian Earth Sciences, 15, 517–531.

McCall, G.J.H., 2002, A summary of the geology of the Iranian Makran. In: Clift, P.D., Kroon, F.D., Gaedecke, C., Craig, J. (Eds.), The Tectonic and Climatic Evolution of the Arabian Sea Region. Special Publication of the Geological Society of London, 95, 147 204.

Merzbacher, C., and Eggler, D.H., 1984, A magmatic geohygrometer: Application to Mount St. Helens and other dacitic magmas: Geology, v. 12, p. 587–590.

Mirnejad, H., Hassanzadeh, J., Cousens, B.L., and Taylor, B.E., 2010, Geochemical evidence for deep mantle melting and lithospheric delamination as the origin of the inland Damavand volcanic rocks of northern Iran: Journal of Volcanology and Geothermal Research, v. 198, p. 288–296.

Mountain, G.S., and Prell, W.L., 1990, A Multiphase Plate Tectonic History of the Southeast Continental Margin of Oman. In A.H.F. Robertson, M.P. Searle and A.C. Ries (Eds.), The Geology and Tectonics of the Oman Region. Geological Society London Special Publication, 49, 725-743.

Müntener, O., and Ulmer, P., 2006, Experimentally derived high-pressure cumulates from hydrous arc magmas and consequences for the seismic velocity structure of lower arc crust. Geophysical Research Letters 33 (21), L21308.

Musson, R.M.W., 2009, Subduction in the western Makran: the historian's contribution, Journal of Geological Society of London, 166, 387-391.

Naney, M.T., 1983, Phase equilibria of rock-forming ferromagnesian silicates in granitic systems: American Journal of Science, v. 283, p. 993–1033.

Pang, K.-N., Chung, S.-L., Zarrinkoub, M.H., Lin, Y.-C., Lee, H.-Y, Lo, C.-H., and Khatib, M.M., 2013, Iranian ultrapotassic volcanism at ~11 Ma signifies the initiation of post-collisional magmatism in the Arabia–Eurasia collision zone: Terra Nova, v. 25, p. 405–413.

Pang, K., Chung, S., Zarrinkoub, M., Chiu, H., and Li, X., 2014, On the magmatic record of the Makran arc, southeastern Iran: Insights from zircon U-Pb geochronology and bulk-rock geochemistry. Geochemistry, Geophysics, Geosystems, 15, doi:10.1002/2014GC005262.

Pearce, J.A., and Peate, D.W., 1995, Tectonic implications of the composition of volcanic arc magmas: Annual Review of Earth and Planetary Sciences, v. 23, p. 251–285.

Peccerillo, A., and Taylor, S.R., 1976, Geochemistry of Eocene calc-alkaline volcanic rocks of the Kastamonu area, northern Turkey. Contribution Mineralogy and Petrology, 58, 63 81.

Perelló, J., Razique, A., Schloderer, J., and Asad-ur-Rehman, 2008, The Chagai Porphyry Copper Belt, Baluchistan Province, Pakistan Economic Geology, 103, 1583-1612.

Putirka, K., 2016, Amphibole thermometers and barometers for igneous systems and some implications for eruption mechanisms of felsic magmas at arc volcanoes. American Mineralogist, 101, 841-858.

Ravaut, P., Bayer, R., Hassani, R., Rousset, D., Al Yahya'ey, A., 1997, Structure and evolution of the northern Oman margin: gravity and seismic constraints over the Zagros-Makran-Oman collision zone, Tectonophysics, 279, 253-280.

Regard, V., Bellier, O., Thomas, J.-C., Abbassi, M.R., Mercier, J., Shabanian, E., Feghhi, K., and Soleymani, S., 2004, Accommodation of Arabia-Eurasia convergence in the Zagros-Makran transfer zone, SE Iran: A transition between collision and subduction through a young deforming system: Tectonics, v. 23, No. 4, TC4007: 10.1029/2003TC001599.

Richards, J.P., 2003, Tectono-magmatic precursors for porphyry Cu–(Mo–Au) deposit formation. Economic Geology 98, 1515–1533.

Richards, J.P., 2009, Postsubduction porphyry Cu-Au and epithermal Au deposits: Products of remelting of subduction-modified lithosphere: Geology, v. 37, p. 247–250.

Richards, J.P., 2011, High Sr/Y arc magmas and porphyry Cu ± Mo ± Au deposits: just add water. Economic Geology 106, 1075–1081.

Richards, J.P., 2015, Tectonic, magmatic, and metallogenic evolution of the Tethyan orogen: From subduction to collision. Ore Geology Reviews, 70, 323–345.

Richards, J.P., and Kerrich, R., 2007, Adakite-like rocks: Their diverse origins and questionable role in metallogenesis: Economic Geology, 102, 537–576.

Richards, J.P., and Sholeh, A., 2016, The Tethyan tectonic history and Cu-Au metallogeny of Iran, *in* Richards, J.P. ed., Tectonics and Metallogeny of the Tethyan Orogenic Belt: Society of Economic Geologists Special Publication No. 19, 193–212.

Richards, J.P., Spell, T., Rameh, E., Razique, A., and Fletcher, T., 2012, High Sr/Y magmas reflect arc maturity, high magmatic water content, and porphyry Cu ± Mo ± Au potential: Examples from the Tethyan arcs of central and eastern Iran and western Pakistan: Economic Geology, 107, 295–332.

Richards, J.P., Jourdan, F., Creaser, R.A., Maldonado, G., and DuFrane, A., 2013, Geology, geochemistry, geochronology, and economic potential of Neogene volcanic rocks in the Laguna Pedernal and Salar de Aguas Calientes segments of the Archibarca lineament, northwest Argentina: Journal of Volcanology and geothermal research, 258, 47–73.

Ridolfi, F., Renzulli, A., and Puerini, M., 2010, Stability and chemical equilibrium of amphibole in calc-alkaline magmas: An overview, new thermobarometric formulations and application to subduction-related volcanoes: Contributions to Mineralogy and Petrology, 160, 45–66.

Rutherford, M.J., and Devine, J.D., 1988, The May 18, 1980, eruption of Mount St. Helens. 3. Stability and chemistry of amphibole in the magma chamber: Journal of Geophysical Research, v. 93, p. 11,949–11,959.

Rutherford, M.J., and Hill, P.M., 1993, Magma ascent rates from amphibole breakdown.an experimental study applied to the 1980-1986 Mount St Helens eruptions. Journal of Geophysical Research Solid Earth, 98, 19667-19685.

Saadat, S., and Stern, C.R., 2011, Petrochemistry and genesis of olivine basalts from small monogenetic parasitic cones of Bazman stratovolcano, Makran arc, southeastern Iran: Lithos, v. 125, p. 607–619.

Shafiei, B., Haschke, M., Shahabpour, J., 2009, Recycling of orogenic arc crust triggers porphyry Cu mineralization in Kerman Cenozoic arc rocks, southeastern Iran: Mineralium Deposita, 44, 265–283.

Shahabpour, J., 2010, Tectonic implications of the geochemical data from the Makran igneous rocks in Iran: Island Arc, v. 19, p. 676-689.

Sholeh, A., Rastad, E., Huston, D., Gemmell, J.B., and Taylor, R.D., 2016, The Chahnaly low-sulfidation epithermal gold deposit, Western Makran Volcanic Arc, Southeast Iran: Economic Geology, v. 111, p. 619–639.

Siddiqui, R.H., 2004, Crustal evolution of Chagai-Raskoh arc terrane, Balochistan, Pakistan: Unpublished Ph.D. thesis, University of Peshawar, 353 p.

Siddiqui, R.H., AsifKhan, M., and Qasim Jan, M., 2007, Geochemistry and petrogenesis of the Miocene alkaline and sub-alkaline volcanic rocks from the Chagai Arc, Baluchistan, Pakistan: Implications for porphyry Cu-Mo-Au deposits, Journal of Himalayan Earth Sciences, 40, 1-23.

Sillitoe, R.H., 1979, Some thoughts on gold-rich porphyry copper deposits: Mineralium Deposita, v. 14, p. 161-174.

Sillitoe, R.H., 2010. Porphyry copper systems. Economic Geology 105, 3–41.

Sillitoe, R.H., and Khan, S.N., 1977, Geology of the Saindak porphyry copper deposit, Pakistan: Transactions Institution of Mining & Metallurgy, v. 86, B27–42.

Spencer, K.J., and Lindsley, D.H., 1981, A solution model for coexisting iron-titanium oxides: American Mineralogist, v. 66, p. 1189–1201.

Sun, S.S., and McDonough, W.F., 1989, Chemical and isotopic systematics of oceanic basalts: implications for mantle composition and processes. In: Saunders, A.D., Norry, M.J. (Eds.), Magmatism in the Ocean Basins, vol. 42. Geological Society of London, Special Publication, 313–345.

Wellman, H.W., 1966, Active wrench faults of Iran, Afghanistan, and Pakistan, Geologische Rundschau, 55(3), 716-735.

Whitmarsh, R.B., 1979, The Owen Basin off the south-east margin of Arabia and the evolution of the Owen Fracture Zone: Geophysical Journal International, v. 58, p. 441–470.

Figure Captions

Fig. 1: Simplified geological map of Iran and different tectonic segments (modified from Richards and Sholeh, 2016).

Fig. 2: Tectonic setting of the Makran subduction zone and the location of Neogene–Quaternary volcanoes. Background image from ETOPO1, http://noaa.gove/mgg/global/relief/ETOPO1/image/color_etopo1_ice_full.tif.gz.

Fig. 3: Geologic map of southeastern Iran and western Pakistan, showing the main Mesozoic and Cenozoic tectonic units and igneous rocks of the Makran volcanic arc and associated porphyry and epithermal deposits. Symbol sizes indicate relative deposit size. Modified from Richards and Sholeh (2016).

Fig. 4: Geological map of the Taftan volcanic complex showing the locations of samples collected for this study; based on the Nuk Abad and Taftan 1:100,000 geological map sheets (Geological Survey of Iran, 1984a,b) and this study. Numbers in legend boxes represent lithological groups used in text.

Fig. 5: (A) The current Taftan edifice includes the Narkuh and Madarkuh vents, with fumarolic activity at Madarkuh [photograph taken from 41R 316507E, 316577N, looking northeast]. (B) Pliocene volcaniclastic deposits overlying Cretaceous–Eocene volcanosedimentary rocks in valley section near Kharestan: lahars and tuffs are covered by younger andesitic lava [photograph taken from 41R 299034E, 3176350N, 2192 m, looking east]. (C) Ignimbrite filling valley on east flank of the Taftan volcano [photograph taken from 41R 0328137E, 3164685N, 1935 m, near sample 13AR017]. (D) Collapsed crater on the southwest side of Taftan volcano, with fumarole in foreground [photograph taken from 41R 317594E, 3165375N, looking southwest].

Fig. 6: Hydrothermal alteration zones within the TVC (Google Earth view): the Kharestan and Bidester porphyry Cu prospects occur in older (Miocene) sequences at the NW end of the complex, whereas shallow argillic, advanced argillic, and fumarolic alteration zones occur around the Quaternary edifice to the SE.

Fig. 7: Hydrothermal alteration in the Kharestan and Bidester Cu porphyry prospects: (A) phyllic, argillic, and advanced argillic alteration exposed in valley bottom at Kharestan [photograph looking west from 41R 298578E, 3177639N, 2184 m]; (B) phyllic alteration at Bidester unconformably overlain by younger, unaltered volcanic sequences [photograph looking south from 41R 0301248E, 3171488N, 2431 m]; (C) oxidized pyrite stockwork in phyllic alteration with argillic alteration overprint at Kharestan [41R 297612E, 3177301N, 2165 m] and (D) Bidester [41R 0301376E, 3171557N, 2440 m]; (E) alunite and jarosite on fracture surfaces in advanced argillic-altered volcanic rock at Kharestan [sample 12AR-010; 41R 298442E, 3176272N, 2216 m] and (F) Bidester [sample BID-1; 41R 0301860E, 3172299N, 2530 m]; (G) siliceous lithocap formed in volcanic rocks overlying Bidester porphyry system [photograph looking north from 41R 0301248E, 3171488N, 2431 m]; (H) secondary malachite and chalcocite in boulder from gully at Bidester [41R 0301760E 3171976N, 2471 m].

Fig. 8: (A) Argillic to advanced argillic hydrothermal alteration zone ~10 km to WNW of Taftan volcano [41R 309904E, 3169289N, 2723 m, looking to ESE]; (B) active fumaroles and fumarolic alteration around the Taftan summit [41R 0317100E, 3165150N, ~3800 m, looking southeast].

Fig. 9: $^{40}Ar/^{39}Ar$ apparent age spectra for minerals from the TVC: (A) sample 12AR010: hydrothermal alunite sample from the Kharestan porphyry deposit; (B) sample BID-1: hydrothermal alunite from the Bidester porphyry deposit; (C) sample 12AR017: igneous biotite from Group 1 late Miocene andesite; (D) sample 13AR006: igneous biotite from Group 3 late Pliocene andesite lava flow; (E) sample 13AR008: igneous biotite from Group 3 late Pliocene andesite lava flow; (F) sample 13AR016: igneous biotite from pumice block in Group 5 Pleistocene andesitic ignimbrite; (G) sample 13AR017: igneous amphibole from pumice block in Group 6 Quaternary andesitic ignimbrite; (H) sample 12AR029: igneous amphibole from andesitic clast in block-and-ash flow, Bazman volcano.

Fig. 10: Photomicrographs of volcanic rocks from the TVC: (A) subhedral to euhedral plagioclase, amphibole (with partially oxidized rims), and pyroxene phenocrysts in late Miocene andesite (sample 12AR017); (B) large sieve-textured plagioclase phenocryst

from Pliocene dacite (sample 13AR007); (C) partially devitrified groundmass with sieve-textured plagioclase, biotite, and embayed quartz phenocrysts (sample 13AR007); (D) subhedral to euhedral oscillatory zoned plagioclase, and amphibole phenocrysts with partially oxidized rims from Pliocene andesite (sample 13AR008); (E) amphibole-plagioclase enclave in Plio-Pleistocene dacite (sample 12AR020); (F) flattened pumice clasts (fiammé) in Quaternary andesitic tuff (sample 13AR017). Abbreviations: Amph = amphibole, Biot = biotite, Chl = chlorite, Cpx = clinopyroxene, Op = opaque mineral, Opx = orthopyroxene, Plag = plagioclase, Qtz = quartz.

Fig. 11: (A) Back scattered electron image of magnetite and ilmenite grains in dacite from Bazman volcano (sample 12AR030); (B) amphibole crystal containing plagioclase inclusions from Pliocene andesite (13AR013); (C) amphibole crystal with thin opacitic rim (Fe-Ti oxides) and internal zoning in Pleistocene andesite (13AR016); (D) completely decomposed amphibole (opacite) in Pliocene dacite (13AR007). Abbreviations: Ilm = ilmenite, Mt = magnetite.

Fig. 12: Classification diagram (Hawthorne et al., 2012) for the calcium amphiboles from the Taftan and Bazman volcanoes showing the average compositions for each sample listed in Table 4. All of the average analyses correspond to magnesio-hastingsite (the ferric analogue of pargasite).

Fig. 13: Geochemical classification of the Taftan and Bazman volcanic rocks: (A) total alkali versus silica diagram (TAS; Le Maitre, 1989); (B) K_2O versus SiO_2 (Peccerillo and Taylor, 1976). Data from Pang et al. (2014) indicated in legend.

Fig. 14: Harker diagrams for major and minor element constituents of the Taftan and Bazman volcanic rocks.

Fig. 15: Plots of trace element data for volcanic rocks from the (A) Taftan and (B) Bazman volcanoes, normalized to primitive mantle composition of Sun and McDonough (1989). Background data ranges are shown for the early Miocene Jebal Barez suite from the Kerman Belt (blue), and the mid-Miocene Kuh Panj suite from the Kerman belt combined with the Neogene Reko Diq and Saindak suites from the Chagai Arc in Pakistan (green).

Data for the Kerman Belt are from Shafiei et al. (2009; excluding samples AP and GCH-1, which have anomalously low HREE and K, respectively), and data for the Chagai Arc are from Richards et al. (2012).

Fig. 16: Plots of rare earth element data for volcanic rocks from the (A) Taftan and (B) Bazman volcanoes, normalized to C1 chondrite composition of Sun and McDonough (1989). Background data ranges are shown for the early Miocene Jebal Barez suite from the Kerman Belt (blue), and the mid-Miocene Kuh Panj suite from the Kerman belt combined with the Neogene Reko Diq and Saindak suites from the Chagai Arc in Pakistan (green). Data for the Kerman Belt are from Shafiei et al. (2009; excluding samples AP and GCH-1, which have anomalously low HREE and K, respectively), and data for the Chagai Arc are from Richards et al. (2012).

Fig. 17: Log oxygen fugacity vs. temperature diagram showing the FMQ buffer at 1 kbar and the average mineral data with 1σ error bars.

Fig. 18: Whole-rock SiO_2 vs. crystallization temperature and ΔFMQ derived from amphibole phenocryst compositions (see text for details).

Fig. 19: Plot of Sr/Y vs. La/Yb for samples from the Taftan and Bazman volcanic complexes, with the range of data from fertile Neogene magmas from the Kerman belt in Iran, and the Chagai belt in Pakistan shown for comparison (data from Shafiei et al., 2009, and Richards et al., 2012).

Table 1. Summary of $^{40}Ar/^{39}Ar$ results and sample descriptions

Sample #	UTM location (41R)	Stratigraphic Group	Plateau age (± 2 s.d.)	Description
12AR010	0298442E, 3176272N, 2216 m		6.10 ± 0.80 Ma	Alunite from advanced argillic alteration, Kharestan porphyry–epithermal deposit
12AR017	0298952E, 3173582N, 2395 m	1	7.87 ± 0.14 Ma	Biotite from late Miocene andesitic lava flow
12AR029	0216656E, 3107195N, 1534 m	Bazman	No plateau: total gas age = 1.9 ± 0.3 Ma	Amphibole from dacitic clast in block-and-ash flow, Bazman volcano
13AR006	0317140E, 3174993N, 2182 m	3	3.10 ± 0.06 Ma	Biotite from late Pliocene andesitic lava flow
13AR008	0310624E, 3170173N, 2709 m	3	2.67 ± 0.08 Ma	Biotite from late Pliocene andesitic lava flow
13AR016	0331667E, 3164814N, 1783 m	5	1.00 ± 0.08 Ma	Biotite from pumice block in Pleistocene andesitic ignimbrite
13AR017	0328108E, 3164668N, 1935 m	6	No plateau: weighted mean age of 8 steps = 404 ± 82 ka	Amphibole from pumice block in Quaternary andesitic ignimbrite
BID-1	0301860E, 3172299N, 2530 m		No plateau: weighted mean age of 6 steps = 4.34 ± 0.04 Ma	Alunite from advanced argillic alteration, Bidester porphyry–epithermal deposit

Table 2. Average pyroxene compositions.

Sample	12AR020-OPX	12AR030-OPX	12AR032-OPX	13AR003-OPX	13AR014-OPX	13AR017-OPX	13AR018-OPX
# points	4	9	3	10	5	7	7
SiO_2	52.76 (0.58)	53.69 (0.57)	53.42 (0.79)	53.47 (0.54)	52.89 (0.84)	53.48 (0.22)	53.25 (0.37)
TiO_2	0.15 (0.02)	0.14 (0.05)	0.15 (0.07)	0.11 (0.03)	0.13 (0.02)	0.14 (0.03)	0.10 (0.02)
Al_2O_3	0.72 (0.17)	0.94 (0.21)	1.22 (0.43)	0.76 (0.20)	0.79 (0.23)	0.79 (0.09)	0.78 (0.23)
Cr_2O_3							
Fe_2O_3	2.20 (0.83)	1.50 (0.67)	1.30 (0.89)	1.68 (0.66)	2.06 (1.69)	2.10 (0.28)	2.06 (0.70)
FeO	17.81 (0.92)	18.71 (0.84)	19.68 (0.72)	19.52 (1.75)	18.70 (1.37)	18.55 (0.35)	19.19 (0.68)
MnO	0.83 (0.04)	0.76 (0.11)	0.80 (0.06)	1.02 (0.41)	0.92 (0.06)	0.93 (.04)	1.03 (0.11)
MgO	24.11 (0.59)	24.46 (0.56)	23.90 (0.31)	23.72 (1.31)	23.95 (0.23)	24.45 (0.31)	23.89 (0.40)
CaO	1.20 (0.68)	0.90 (0.28)	0.73 (0.08)	0.93 (0.24)	0.76 (0.07)	0.77 (0.04)	0.75 (0.06)
Na_2O							
Total	99.78 (0.52)	101.10 (0.42)	101.20 (0.33)	101.21 (0.47)	100.20 (0.62)	101.21 (0.26)	101.05 (0.19)
Si	1.950	1.956	1.952	1.958	1.951	1.950	1.952
Ti	0.004	0.004	0.004	0.003	0.004	0.004	0.003
Al	0.031	0.040	0.053	0.033	0.034	0.034	0.034
Cr							
Fe^{3+}	0.061	0.041	0.036	0.046	0.057	0.058	0.057
Fe^{2+}	0.551	0.570	0.601	0.598	0.577	0.566	0.588
Mn	0.026	0.023	0.025	0.032	0.029	0.029	0.032
Mg	1.329	1.329	1.302	1.295	1.317	1.329	1.305
Ca	0.048	0.035	0.029	0.036	0.030	0.030	0.029
Na							

Mg#	67.6 (0.7)	67.7 (1.4)	66.3 (0.4)	65.7 (3.4)	66.5 (0.4)	67.1 (0.6)	65.8 (0.8)

One-sigma standard deviations given in parentheses.

Proportions of FeO and Fe_2O_3 calculated on the basis of 4 cations and 6 oxygen following Droop (1987).

Mg# = 100*Mg/(Mg+Mn+Fe^{2+}+Fe^{3+}) on a molar basis.

Table 3. Average compositions of magnetite-ilmenite pairs.

Sample	12AR013-MAG1	12AR013-ILM1	12AR013-MAG2	12AR013-ILM2	12AR013-MAG3-1	12AR013-ILM3-1	12AR013-MAG4	12AR013-ILM4
mineral	magnetite	ilmenite	magnetite	ilmenite	magnetite	ilmenite	magnetite	ilmenite
# points	3	3	4	2	1	1	5	3
MgO	0.74	4.13	0.37	1.80	1.21	0.07	0.59	2.05
Al_2O_3	1.64	0.15	1.14	0.20	1.42	0.14	1.81	0.16
SiO_2	0.16	0.05	0.10	0.03	0.11	0.32	0.15	0.05
CaO	0.07	0.07	0.06	0.03	0.06	0.10		0.06
TiO_2	4.14	44.70	1.77	40.76	4.24	43.88	3.58	45.13
Cr_2O_3	0.17	0.06	0.16				0.12	0.04
MnO	0.21	1.84	0.09	1.07	0.32	0.14	0.20	1.31
FeO	33.72	30.96	32.13	32.37	32.51	39.46	33.52	35.60
Fe_2O_3	58.40	17.87	63.70	23.18	58.19	12.98	59.21	14.97
Total	99.25	99.83	99.52	99.44	98.06	97.09	99.18	99.37
Mg	0.126	0.608	0.063	0.272	0.208	0.011	0.101	0.308
Al	0.221	0.017	0.154	0.024	0.193	0.017	0.244	0.019
Si	0.018	0.005	0.011	0.003	0.013	0.033	0.017	0.005
Ca	0.009	0.007	0.007	0.003	0.007	0.011		0.006
Ti	0.356	3.320	0.153	3.103	0.368	3.448	0.308	3.417
Cr	0.015	0.005	0.015				0.011	0.003
Mn	0.020	0.154	0.009	0.092	0.031	0.012	0.019	0.112
Fe^{2+}	3.219	2.556	3.085	2.739	3.134	3.447	3.205	2.996
Fe^{3+}	5.016	1.328	5.503	1.765	5.047	1.020	5.095	1.134
mean T (°C)		777 (6)		734 (1)		743 (11)		751 (3)
mean log fO_2		-12.9 (0.2)		-13.0 (0.1)		-14.0 (0.1)		-13.6 (0.

One-sigma standard deviations of calculations given in parentheses.

Proportions of FeO and Fe_2O_3 calculated on the basis of 12 oxygen following Droop (1987).

Table C. Continued.

Sample	12AR030-MAG2	12AR030-ILM2	12AR030-MAG3	12AR030-ILM3	12AR032-MAG1	12AR032-ILM1	13AR003-MAG4	13AR003-ILM4
mineral	magnetite	ilmenite	magnetite	ilmenite	magnetite	ilmenite	magnetite	ilmenite
# points	3	2	4	2	3	2	4	4
MgO	1.27	1.82	1.69	2.15	1.16	3.31	1.46	3.73
Al_2O_3	2.50	0.37	2.41	0.64	2.00	0.25	2.11	0.13
SiO_2	0.11	0.08	0.20	0.27	0.06		0.09	0.09
CaO	0.05	0.03	0.05	0.04	0.07			0.05
TiO_2	7.20	37.68	7.91	37.22	2.90	41.22	10.77	47.23
Cr_2O_3	0.15	0.03	0.14	0.06	0.14	0.03	0.07	0.02
MnO	0.45	0.47	0.40	0.42	0.18	0.64	0.34	0.57
FeO	35.55	30.23	35.86	29.50	31.90	30.53	38.82	35.30
Fe_2O_3	51.76	28.52	50.84	29.53	60.92	24.35	45.91	12.65
Total	99.04	99.23	99.50	99.83	99.33	100.33	99.57	99.77
Mg	0.214	0.276	0.283	0.322	0.197	0.489	0.244	0.550
Al	0.333	0.044	0.318	0.076	0.268	0.029	0.279	0.015
Si	0.012	0.008	0.022	0.027	0.007		0.010	0.009
Ca	0.006	0.003	0.006	0.004	0.009			0.005
Ti	0.612	2.879	0.667	2.815	0.248	3.076	0.909	3.512
Cr	0.013	0.002	0.012	0.005	0.013	0.002	0.006	0.002
Mn	0.043	0.040	0.038	0.036	0.017	0.054	0.032	0.048
Fe^{2+}	3.361	2.568	3.363	2.480	3.032	2.532	3.643	2.918
Fe^{3+}	4.404	2.180	4.290	2.234	5.210	1.817	3.876	0.941
mean T (°C)		864 (4)		872 (10)		761 (15)		829 (6)
mean log fO_2		-11.2 (0.1)		-11.1 (0.1)		-12.6 (0.1)		-13.0 (0.

Table C. Continued.

Sample	13AR006-MAG3	13AR006-ILM3	13AR018-MAG1	13AR018-ILM1
mineral	magnetite	ilmenite	magnetite	ilmenite
# points	2	2	4	4
MgO	0.86	1.39	0.38	2.62
Al_2O_3	2.67	0.48	1.31	0.17
SiO_2	0.12	0.12	0.10	0.08
CaO	0.23	0.11	0.11	0.11
TiO_2	7.85	35.80	0.69	41.62
Cr_2O_3	0.07	0.04	0.12	0.04
MnO	0.44	0.40	0.04	0.54
FeO	36.74	29.32	30.75	32.18
Fe_2O_3	50.42	32.47	64.80	21.59
Total	99.40	100.13	98.30	98.95
Mg	0.145	0.209	0.066	0.394
Al	0.355	0.057	0.179	0.020
Si	0.014	0.012	0.012	0.008
Ca	0.028	0.012	0.014	0.012
Ti	0.666	2.723	0.060	3.160
Cr	0.006	0.003	0.011	0.003
Mn	0.042	0.034	0.004	0.046
Fe^{2+}	3.465	2.479	2.988	2.716
Fe^{3+}	4.279	2.470	5.666	1.640
mean T (°C)		887 (5)		676 (4)
mean log fO_2		-10.8 (0.1)		-13.7 (0.1)

Table 4. Average amphibole compositions, calculated temperatures and oxygen fugacities.

Sample	12AR013-AMPH	12AR017-AMPH	12AR020-AMPH	12AR030-AMPH
# points	6	22	18	15
SiO_2	41.08 (0.32)	41.14 (0.57)	44.60 (1.64)	44.66 (2.22)
TiO_2	2.65 (0.17)	3.35 (0.24)	1.77 (0.18)	2.09 (0.54)
Al_2O_3	14.16 (0.19)	13.41 (0.65)	9.00 (1.59)	10.62 (2.05)
Cr_2O_3	0.01 (0.02)		0.04 (0.12)	0.01 (0.03)
MnO	0.12 (0.02)	0.15 (0.04)	0.37 (0.07)	0.22 (0.06)
FeO	3.58 (0.83)	5.36 (1.38)	8.64 (1.52)	7.62 (1.12)
Fe_2O_3	7.83 (1.12)	6.87 (0.52)	5.24 (1.44)	5.58 (1.21)
MgO	14.78 (0.23)	13.91 (0.74)	14.00 (1.11)	14.56 (0.78)
CaO	11.90 (0.10)	11.55 (0.16)	11.51 (0.22)	11.15 (0.22)
Na_2O	2.45 (0.11)	2.44 (0.10)	1.66 (0.20)	1.89 (0.43)
K_2O	0.81 (0.03)	1.02 (0.06)	0.85 (0.13)	0.34 (0.04)
H_2O+	1.15 (0.20)	1.12 (0.06)	1.39 (0.04)	1.49 (0.11)
F	0.66 (0.36)	0.33 (0.07)	0.44 (0.05)	0.19 (0.04)
Cl	0.01 (0.02)	0.02 (0.03)	0.12 (0.04)	0.04 (0.03)
O=F,Cl	-0.28 (0.15)	-0.14 (0.03)	-0.21 (0.02)	-0.09 (0.02)
Total	100.90 (0.32)	100.53 (0.32)	99.41 (0.72)	100.37 (0.56)
Si	5.950	6.027	6.606	6.492
^{T}Al	2.050	1.973	1.394	1.508
^{C}Al	0.367	0.342	0.177	0.311
Ti	0.289	0.369	0.197	0.229
Cr	0.001		0.005	0.001
Fe^{3+}	0.853	0.758	0.583	0.610
$^{C}Fe^{2+}$	0.299	0.492	0.947	0.694

Mg	3.191	3.038	3.091	3.155
^{B}Mn	0.015	0.019	0.046	0.027
$^{B}Fe^{2+}$	0.134	0.163	0.123	0.232
Ca	1.847	1.813	1.827	1.737
^{B}Na	0.004	0.005	0.004	0.004
^{A}Na	0.684	0.688	0.473	0.528
K	0.150	0.191	0.161	0.063
sum cations	15.834	15.878	15.634	15.591
OH	1.117	1.103	1.369	1.445
F	0.302	0.153	0.206	0.087
Cl	0.002	0.005	0.030	0.010
O	0.578	0.739	0.395	0.458
mean T (°C)	1026 (7)	1009 (18)	878 (40)	903 (60)
mean log fO_2	-8.9 (0.1)	-9.6 (0.3)	-11.1 (0.6)	-10.6 (0.7)

One-sigma standard deviations given in parentheses.

Formulae calculated on the basis of 24 (OH,O,F,Cl), with proportions of FeO and Fe_2O_3 calculated on the basis of ΣSi-to-Ca <= 15 apfu, and hydroxyl calculated as OH=2-2*Ti apfu (Hawthorne et al., 2012).

Table 4. Continued.

Sample	13AR006-AMPH	13AR007-AMPH	13AR010-AMPH	13AR012-AMPH
# points	27	33	19	12
SiO_2	44.49 (1.18)	43.02 (1.61)	45.56 (1.54)	43.36 (0.69)
TiO_2	1.53 (0.35)	2.16 (0.30)	1.80 (0.20)	2.40 (0.37)
Al_2O_3	10.03 (1.19)	12.02 (1.71)	9.46 (1.67)	12.60 (1.36)
Cr_2O_3	0.02 (0.06)	0.01 (0.03)		0.04 (0.03)
MnO	0.36 (0.12)	0.17 (0.11)	0.28 (0.03)	0.14 (0.06)

FeO	10.73 (3.28)	5.94 (2.18)	8.08 (0.76)	6.04 (2.34)
Fe_2O_3	5.06 (1.02)	6.55 (1.00)	5.08 (0.76)	5.32 (0.67)
MgO	12.69 (1.78)	14.37 (1.25)	14.75 (0.72)	14.91 (1.04)
CaO	11.61 (0.17)	11.89 (0.19)	11.48 (0.13)	11.67 (0.23)
Na_2O	1.55 (0.22)	2.02 (0.28)	1.63 (0.21)	2.35 (0.23)
K_2O	0.91 (0.29)	0.73 (0.16)	0.69 (0.08)	0.64 (0.07)
H_2O+	1.53 (0.06)	1.46 (0.05)	1.47 (0.05)	1.37 (0.14)
F	0.27 (0.04)	0.20 (0.06)	0.33 (0.03)	0.31 (0.10)
Cl	0.09 (0.06)	0.03 (0.03)	0.10 (0.03)	0.02 (0.04)
O=F,Cl	-0.13 (0.02)	-0.09 (0.03)	-0.16 (0.01)	-0.14 (0.05)
Total	100.74 (0.88)	100.48 (0.65)	100.55 (0.40)	101.02 (0.49)

Si	6.546	6.262	6.622	6.255
^{T}Al	1.454	1.738	1.378	1.745
^{C}Al	0.286	0.324	0.243	0.397
Ti	0.169	0.237	0.197	0.260
Cr	0.002	0.001		0.005
Fe^{3+}	0.560	0.717	0.555	0.577
$^{C}Fe^{2+}$	1.199	0.603	0.809	0.554
Mg	2.784	3.118	3.196	3.207
^{B}Mn	0.045	0.021	0.034	0.017
$^{B}Fe^{2+}$	0.121	0.120	0.174	0.174
Ca	1.830	1.854	1.788	1.804
^{B}Na	0.003	0.004	0.004	0.005
^{A}Na	0.439	0.566	0.456	0.653
K	0.171	0.136	0.128	0.118
sum cations	15.609	15.701	15.584	15.771

OH	1.513	1.427	1.430	1.332
F	0.126	0.092	0.152	0.141
Cl	0.022	0.007	0.025	0.005
O	0.339	0.474	0.394	0.522
mean T (°C)	883 (36)	958 (50)	878 (44)	969 (36)
mean log fO_2	-11.3 (0.9)	-9.9 (0.8)	-10.9 (0.5)	-9.7 (0.8)

Table 4. Continued.

Sample	13AR014-AMPH	13AR016-AMPH	13AR017-AMPH
# points	32	44	20
SiO_2	44.38 (1.70)	44.59 (1.72)	46.10 (1.06)
TiO_2	1.91 (0.24)	1.75 (0.28)	1.74 (0.18)
Al_2O_3	10.36 (1.94)	10.63 (2.39)	8.72 (0.65)
Cr_2O_3	0.01 (0.02)	0.01 (0.02)	0.01 (0.02)
MnO	0.25 (0.08)	0.30 (0.16)	0.31 (0.03)
FeO	7.84 (2.12)	8.13 (3.23)	8.65 (0.50)
Fe_2O_3	5.05 (1.09)	4.95 (1.07)	4.61 (0.75)
MgO	14.49 (0.97)	14.36 (1.58)	14.83 (0.51)
CaO	11.45 (0.20)	11.61 (0.22)	11.36 (0.10)
Na_2O	1.93 (0.33)	1.85 (0.34)	1.57 (0.11)
K_2O	0.68 (0.15)	0.78 (0.16)	0.69 (0.08)
H_2O+	1.46 (0.07)	1.53 (0.05)	1.49 (0.05)
F	0.28 (0.08)	0.22 (0.06)	0.31 (0.03)

Cl	0.08 (0.06)	0.08 (0.07)	0.11 (0.02)
O=F,Cl	-0.14 (0.03)	-0.11 (0.03)	-0.16 (0.01)
Total	100.03 (0.88)	100.69 (0.49)	100.33 (0.65)
Si	6.495	6.487	6.716
^{T}Al	1.505	1.513	1.284
^{C}Al	0.282	0.310	0.214
Ti	0.210	0.192	0.191
Cr	0.001	0.001	0.001
Fe^{3+}	0.556	0.543	0.505
$^{C}Fe^{2+}$	0.789	0.840	0.869
Mg	3.161	3.115	3.221
^{B}Mn	0.031	0.037	0.038
$^{B}Fe^{2+}$	0.170	0.149	0.185
Ca	1.795	1.810	1.773
^{B}Na	0.004	0.004	0.004
^{A}Na	0.544	0.518	0.440
K	0.127	0.145	0.128
sum cations	15.670	15.664	15.569
OH	1.429	1.495	1.448
F	0.130	0.101	0.143
Cl	0.020	0.020	0.027
O	0.421	0.384	0.382
mean T (°C)	908 (56)	910 (66)	859 (21)
mean log fO_2	-10.5 (0.9)	-10.5 (1.2)	-11.2 (0.2)

Table 5. Crystallization temperatures and fO_2 conditions estimated from amphibole and magnetite–ilmenite crystal pairs (* from Bazman)

Sample	T (°C)	±1σ	fO_2	±1σ	ΔFMQ at 1 kbar
12AR013-AMPH	1026	7	-8.9	0.1	1.6
12AR017-AMPH	1009	18	-9.6	0.3	1.2
12AR020-AMPH	878	40	-11.1	0.6	1.9
*12AR030-AMPH	903	60	-10.6	0.7	1.9
13AR006-AMPH	883	36	-11.3	0.9	1.6
13AR007-AMPH	958	50	-9.9	0.8	1.7
13AR010-AMPH	878	44	-10.9	0.5	2.1
13AR012-AMPH	969	36	-9.7	0.8	1.7
13AR014-AMPH	908	56	-10.5	0.9	1.9
13AR016-AMPH	910	66	-10.5	1.2	1.9
13AR017-AMPH	859	21	-11.2	0.2	2.2
12AR013-MAG1					
12AR013-ILM1	777	6	-12.9	0.2	2.1
12AR013-MAG2					
12AR013-ILM2	734	1	-13	0.1	3.1
12AR013-MAG3-1					
12AR013-ILM3-1	743	11	-14	0.1	1.9
12AR013-MAG4					
12AR013-ILM4	751	3	-13.6	0.1	2.0
*12AR030-MAG1					
*12AR030-ILM1	862	13	-11.1	0.1	2.2
*12AR030-MAG2					
*12AR030-ILM2	864	4	-11.2	0.1	2.1
*12AR030-MAG3					
*12AR030-ILM3	872	10	-11.1	0.1	2.0
*12AR032-MAG1					
*12AR032-ILM1	761	15	-12.6	0.1	2.8
13AR003-MAG4					
13AR003-ILM4	829	6	-13	0.2	1.0
13AR006-MAG2					
13AR006-ILM2	924	8	-10.2	0.1	2.0
13AR006-MAG3					
13AR006-ILM3	887	5	-10.8	0.1	2.0
13AR018-MAG1					
13AR018-ILM1	676	4	-13.7	0.1	3.8

Highlights

- Taftan and Bazman are the easternmost Miocene–Quaternary arc volcanoes in Iran.
- Rocks are calc-alkaline to high-K calc-alkaline, with normal arc geochemistry.
- Andesitic to dacitic lava flows, ignimbrites, and lahar deposits.
- Similar in composition to the Miocene Kerman belt in Iran.
- Similar in composition to the Miocene–Quaternary Chagai belt in western Pakistan.
- Porphyry Cu±Mo±Au and epithermal Au mineralization is present at Taftan.